Analysis of Flowfields over Four-Engine DC-X Rockets

Ten-See Wang* and Joni Cornelison†
NASA Marshall Space Flight Center, Huntsville, Alabama 35812

The objective of this study is to validate a computational methodology for the aerodynamic performance of an advanced conical launch vehicle configuration. The computational methodology is based on a three-dimensional, viscous flow, pressure-based computational fluid dynamics formulation. Both wind-tunnel and ascent flight-test data are used for validation. Emphasis is placed on multiple-engine power-on effects. Computational characterization of the base drag in the critical subsonic regime is the focus of the validation effort; until recently, almost no multiple-engine data existed for a conical launch vehicle configuration. Parametric studies using high-order difference schemes are performed for the cold-flow tests, whereas grid studies are conducted for the flight tests. The computed vehicle axial force coefficients, forebody, aftbody, and base surface pressures compare favorably with those of tests. The results demonstrate that with adequate grid density and proper distribution, a high-order difference scheme, finite rate afterburning kinetics to model the plume chemistry, and a suitable turbulence model to describe separated flows, plume/air mixing, and boundary layers, computational fluid dynamics is a tool that can be used to predict the low-speed aerodynamic performance for rocket design and operations.

Nomenclature

A = area, m^2
C_{au} = axial force coefficient, $\int (p - p_i) n \, dA/(Q_\infty A_b)$
M = Mach number
n = directional normal
P = pressure, Pa
Q = 0.5 ρu^2, Pa
u = mean velocity in x direction, m/s
ρ = density, kg/m^3

Subscripts

b = base
c = chamber property
e = nozzle exit
i = aeroshell inside property
0 = reference
∞ = freestream or test cell

Introduction

THE goal of the X-33 program, managed by NASA Marshall Space Flight Center (MSFC), is to demonstrate the technology needed to build a low-cost, fully reusable single-stage-to-orbit rocket that will deliver cargo or personnel to orbit and return. Three concepts are being studied by NASA and its industrial partners: the Rockwell winged body, the McDonnell Douglas/Boeing vertical takeoff and landing, and the Lockheed Martin lifting body configuration. One team will be selected to develop its concept into an experimental flying rocket by 1999.

In this work, computational fluid dynamics (CFD) validation of the subsonic aerodynamic performance of McDonnell Douglas/Boeing team's design, the Delta Clipper-Experimental (DC-X) rocket, is reported. The four-engine (RL10A5) single-stage DC-X rocket is a flying technology testbed that demonstrates technology for NASA's reusable launch vehicle program. Knowledge gained in developing and flight testing the DC-X can be used in development of the X-33 advanced technology demonstrator and, ultimately, in a full-scale reusable launch vehicle.

Presented as Paper 96-2953 at the AIAA/ASME/SAE/ASEE 32nd Joint Propulsion Conference, Lake Buena Vista, FL, July 1–3, 1996; received Aug. 8, 1996; revision received April 15, 1997; accepted for publication June 28, 1997.

*Team Leader, Computational Analysis Team. Member AIAA.
†Aerospace Engineer, Fluid Dynamics Analysis Branch.

For launch vehicles using clustered engines, it is well known that the base environment significantly affects the overall drag[1,2] and integrity[3] of these vehicles. Hence, it becomes very important to be able to predict the base drag during the vehicle design phase. Although empirical equations[4] and wind-tunnel and historical flight-test data are still an integral part of the design process, CFD-based methods have emerged as a new tool. When properly anchored, these CFD-based methods can reduce the inherent uncertainties,[1,5,6] high costs, and impracticality associated with wind-tunnel measurements and flight tests. The DC-X tests are unique in that the flight vehicle and the cold-flow model have satisfied the basics of the scaling law,[2] including similarities in geometry, freestream Mach numbers, and nozzle exit-to-ambient pressure ratios (P_e/P_∞). The cold-flow and flight tests are, therefore, complementary in terms of the measurements. A systematic validation process of both tests presents a unique opportunity to further demonstrate the power of CFD as a design tool to support the X-33 reusable launch vehicle in terms of aerodynamic performance characterization, vehicle design refinement, and optimization.

In an earlier effort, the McDonnell Douglas Navier–Stokes three-dimensional (MDNS3D) CFD code[7] was calibrated for a plug-nozzle DC-X configuration through comparisons with cold-flow data. Also, a separate effort benchmarked the finite difference Navier–Stokes (FDNS) CFD methodology[8,9] with a cold-flow four-engine clustered nozzle base-flow experiment without the influence of the external flow over a vehicle body. In the current study, the FDNS CFD formulation is further benchmarked with the wind-tunnel data for an exact replica of the four-nozzle DC-X rocket. Here, the base-flow physics is complicated by the external flow past the forebody and aftbody. The DC-X ascent flight-test data, where the full-vehicle combined base environment with the hot engine exhaust and afterburning of the excess hydrogen with entrained air, are used to complete the validation process. Previous benchmarks[8,9] have covered a range of P_e/P_∞ from 5 to 510 and equivalent altitudes from 7000 to 37,500 m, whereas the current effort completes the critical lower spectrum of P_e/P_∞ from 1.2 to 1.7, equivalent altitudes from 1500 to 3000 m, and Mach number from 0.1 to 0.3 during ascent at zero angle of attack. Computations were performed to evaluate the forebody, aftbody, and base pressures and the total drag. The effect of afterburning plumes on the base-flow physics is studied, and the scaling practice using cold-flow tests to infer flight vehicle conditions is discussed.

Multiple-Engine Base-Flow Physics

Several excellent reviews on this subject, from which much of the following discussion is abstracted, can be found in the literature.[4,9–11] During vehicle ascent, the blunt rear geometry causes the

Analysis of Flowfields over Four-Engine DC-X Rockets

T.-S. Wang and J. Cornelison

Reprinted from

Journal of Spacecraft and Rockets

Volume 34, Number 5, Pages 620–627

AIAA

A publication of the
American Institute of Aeronautics and Astronautics, Inc.
1801 Alexander Bell Drive, Suite 500
Reston, VA 20191–4344

external flow to separate from the base and to form a near-conic recirculation pattern, which interacts with the exhaust plumes at all times. The amount of the interaction between the external flow and the plumes depends on the degree of plume expansion, which in turn is a function of altitude, flight trajectory, and vehicle speed. In general, at low altitudes aspirating base flow usually occurs where minimal plume-to-external flow and plume-to-plume interactions are seen. At moderate altitudes, plume-to-plume interaction takes place producing a base-impinging reverse jet, which in turn forms a wall jet. The amount of plume-to-plume interaction and, thus, strength of the reverse jet, are functions of the altitude. At high altitudes, the wall jet chokes at a certain point and further reduction in ambient pressure does not alter the base environment. With increasing altitude, the highly expanded plumes are eventually large enough to induce separation of the body boundary layer upstream of the base corner. The multiple-engine base-flow physics are dramatically different from those of the single-engine and power-off projectile base flows, in that a three-dimensional reverse jet is usually formed due to the plume-to-plume interaction at altitudes. The approximate leveling of the nozzle exit planes with the base plane of DC-X configuration implies a vanishing theoretical vent area ratio.[10] Thus, according to the reported base pressure characteristic curves,[10] it is anticipated that the peak base pressures will be higher than those of nonvanishing vent area ratios under similar operating conditions.

Figure 1 shows a representation of important flow features of a four-engine clustered DC-X during ascent flight at low altitudes and subsonic flow speeds. These flow features are a composite distilled from the computational results and the literature.[3,4,11–13] Among the cases studied, including both the wind-tunnel and the flight tests, the strongest plume-to-plume interaction was not strong enough to produce a multiple-engine base-impinging reverse jet. The main base-flow feature studied, hence, is deduced as the aspirating[4] category. At these conditions, the flowfield has an inviscid structure composed of several weak compressions and expansions occurring around the body, including a corner expansion. As the body viscous boundary layer expands around the base corner, a recirculation region is created and a free shear layer is formed that aspirates among the plumes and coalesces at the wake neck and continues downstream as the trailing wake. Inside the plume and in the near field, the moderately underexpanded supersonic jet ($P_e/P_\infty < 1.7$) is characterized by an inviscid shock cell structure with a thin mixing layer developing along the plume and sonic slipstream. For maximum performance, the engines always run fuel rich. Hence, the exhaust plume afterburns along the mixing layer. A transition zone joins the predominantly inviscid near field with the fully viscous, ambient pressure equilibrated far field. In the viscous/inviscid interaction region, the shock cells and wave intensities are gradually dissipated by turbulence and the inviscid core is taken over by the mixing layer. In the far field, wave processes are totally dissipated and constant pressure mixing prevails. It is noted, and was experienced in this study, that damping of wave amplitudes in the transitional region has negligible influence on the solution for base-flow applications.[13] Nevertheless, up to eight shock cells were captured with the typical grids used.

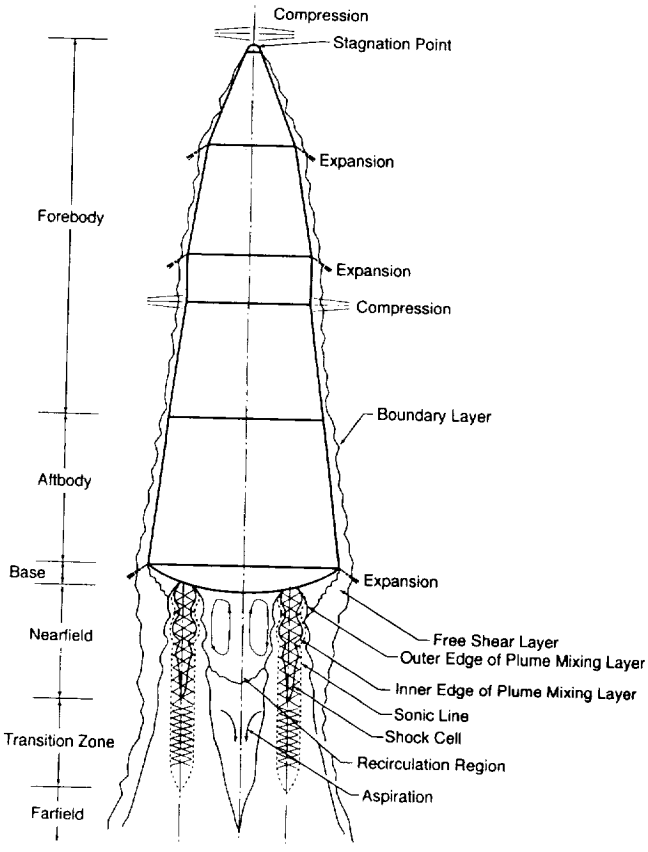

Fig. 1 Schematic of flow features of a DC-X during ascent flight at subsonic speeds.

Solution Methodology

Grid Generation

The cold-flow test article consists of a 5%-subscale replica of the aerodynamic shape of the DC-X vehicle. The model consists of a triconic forebody section having a spherical blunt nose, a quasiconic aftbody section that has flat sides, and a cross section, dubbed a super-circle, that is a square with rounded corners and a slightly curved base. The model is supported by an L-shaped sting support system. The horizontal sting support passes through the base of the model and is supported by a vertical support (not modeled). Because of the symmetrical nature of the flowfield, only $\frac{1}{8}$ of this layout is generated and computed. The symmetry of the flowfield is identified by two symmetry planes[9]: the one that lies between the nozzles is referred to as the plume impingement symmetry plane (PISP) because the plume impingement line will be attached to it, and the other one is termed the nozzle symmetry plane (NSP) because it passes through the centerline of the nozzles in a diagonal position.

In the cold-flow test modeling, the grid density was carefully designed according to earlier cold-flow benchmarks,[9] resulting with a grid B (250,947 points) that was deemed appropriate, as will be shown in later sections. The layout of grid B is shown in Fig. 2. Three

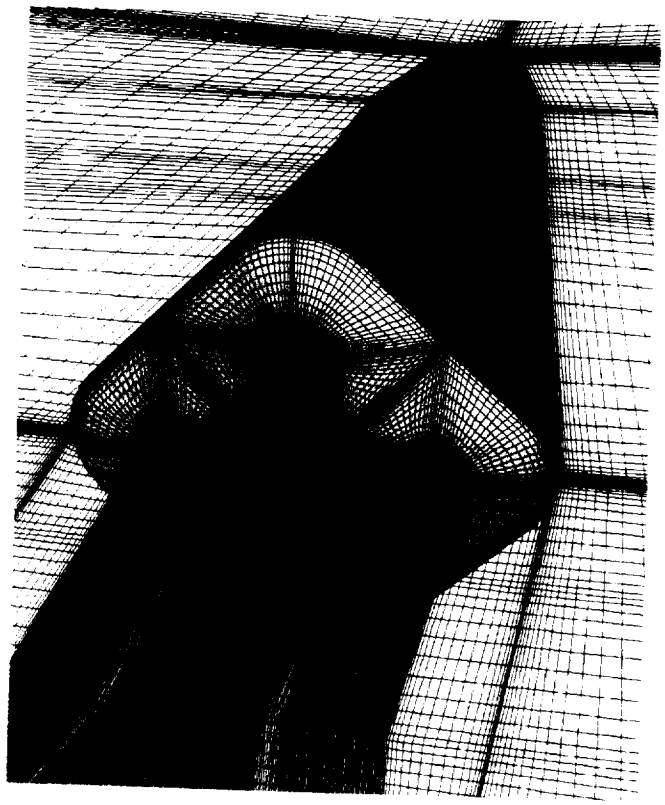

Fig. 2 Layout of a typical exploded full-view computational grid for cold-flow model.

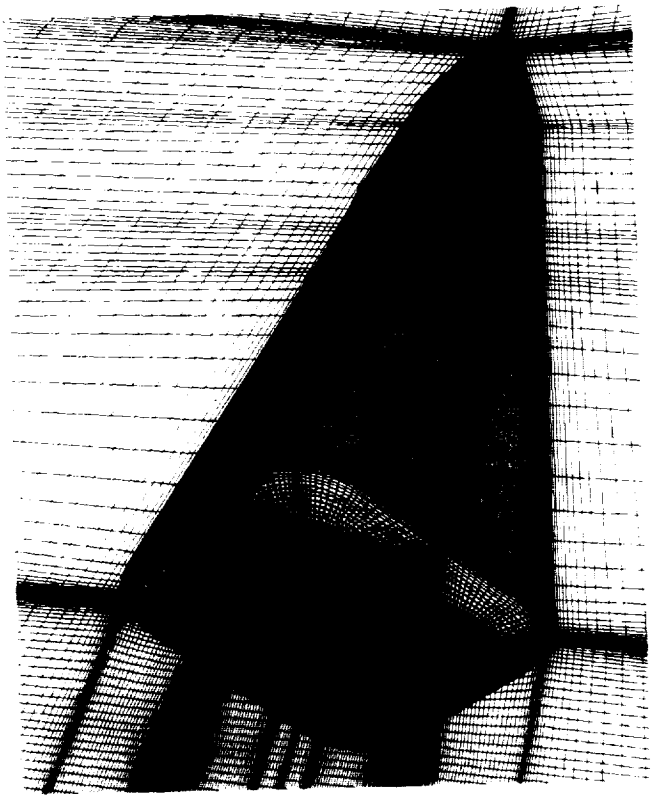

Fig. 3 Layout of a typical exploded full-view computational grid for flight vehicle.

computational grid zones were created. The first zone handles the freestream flow, and the second zone covers the expanding plumes. The third zone resides inside the second zone, covering a thin ring-shaped hole carved on the base to house the sting. The grids were generated with the GENIE++ grid generator.[14] Because the base surface cannot be described by a simple geometry, it is created by projecting a two-dimensional grid-layout onto the actual surface mapping, using the software package GRIDGEN.[15] The four embedded conical nozzles are equally spaced at 90-deg intervals. In addition to the symmetry planes, the grid domain is enclosed by outer surfaces, which are generally positioned at two vehicle lengths from the body, except for the one in front of the nose, which is located at one vehicle-length distance.

A typical grid layout for the flight tests is shown in Fig. 3. Grid F (320,787 points) was generated based on grid B topology, with some extra 76,800 points clustered in the plume shear layer to better capture the anticipated afterburning, and with a zone 3 extended to model the centerline without sting blockage. Initial calculations indicated grids G and H (both at 408,288 points), with more axial points added near the plume impingement line, were necessary for cases with higher plume expansions. Solution-adaptive gridding[9] was not performed because neither forebody shocks nor plume-to-plume recompression was ever formed under the given conditions. The grid densities in the forebody section are identical for both cold-flow and flight-test computations.

Prandtl–Meyer Solution Treatment for Initial Plume Angle Resolution

It has been shown that the initial plume angle grid resolution is essential to the efficient and accurate prediction of base-flow properties.[8,9] The predicted base-flow properties showed vast improvement with fewer grid points when the grid lines extending from the nozzle lip follow an angle according to the isentropic Prandtl–Meyer plume expansion theory.[16] Accordingly, each grid generated in this study has applied the Prandtl–Meyer solution treatment for initial plume angle resolution. The computational efficiency gained from it verifies the inviscid nature[10] of the multiple-engine clustered nozzle base-flow physics. Because of low P_e/P_∞ ratios, the variation (2–6 deg) of the Prandtl–Meyer expansion angles calculated in this study is small compared to that of Ref. 9 (18–53 deg).

Solution Algorithm

Flow solutions about the aerodynamic flowfield over a DC-X full-vehicle configuration with four-engine plume-on effects were generated with the FDNS code.[17] The code was originally developed at MSFC and is continuously being improved by MSFC personnel and its supporting contractors. The code is a pressure-based, general-purpose, Reynolds-averaged transport equations solver, with a variety of options for physical models and boundary conditions. To solve the system of nonlinear partial differential equations, the code uses finite difference approximations to establish a system of linearized algebraic equations. Several difference schemes were employed to approximate the convective terms of the momentum, energy, and continuity equations, including central-difference[18] (CD), upwind (UW), and total-variation-diminishing (TVD) schemes.[19]

Viscous fluxes and source terms are discretized using a CD approximation. A pressure-based predictor plus multiple-corrector solution method is employed so that flow over a wide speed range, from the low subsonic base and freestream flows to the supersonic plume flows, can be efficiently analyzed. The basic idea of this pressure-based method is to perform corrections for the pressure and velocity fields by solving a pressure correction equation so that velocity and pressure coupling is enforced, based on the continuity constraint at the end of each iteration. Details of the present numerical methodology are given in Ref. 18.

An extended two-equation turbulence model[20] closure is used to describe the flow turbulence including flow separation, plume/air mixing, and boundary-layer development. A modified wall function approach[21] is employed by incorporating a complete velocity profile.[22] This complete velocity profile provides a smooth transition between logarithmic law-of-the-wall and linear viscous sublayer velocity distributions.

Boundary Conditions

The nozzle exit flow was carefully prepared with a separate axisymmetric CFD calculation. The computational domain starts from the subsonic chamber, to ensure the correct throat sonic line and, hence, accurate nozzle exit flow properties including internal boundary-layer growth, nozzle shock strength and location, and turbulence level generated from the velocity gradient inside the nozzle. These two-dimensional nozzle exit flow properties were then mapped to the three-dimensional nozzle exit plane in which a fixed inlet boundary is specified. For flight-test validations, a thermo-equilibrium analysis using the CEC code[23] was first performed with RL10A5 engine conditions to establish the chamber inlet flow properties. The ensuing thrust chamber CFD analysis was carried out assuming frozen chemistry. This procedure is critical to the final base-flow solution because the propulsive nozzle flow has a major influence on base-flow phenomena.

The surfaces of the forebody, aftbody, nozzle lip, base, and the sting were specified as no-slip wall boundaries, and a tangency condition was imposed on the symmetry planes. One of the outer surfaces corresponding to the flow exit plane was specified as an exit boundary. In addition, a fixed (ambient) pressure was imposed on a point far away from the action areas, to obtain a unique solution for the corresponding altitude. Two other outer surfaces involving the freestream flow were given ambient total conditions. The pressure link coefficients on the exit plane are established and related to the pressures in the interior. Flow properties at the wall, symmetry plane, and exit boundary were extrapolated from those of the interior.

In the cold-flow benchmarks, several boundary conditions, such as the no-slip walls and symmetry planes, were used parametrically to describe the base holes that house the sting and the nozzles, including a case that modeled the holes as wells with depth. None of the conditions made any noticeable difference in the base drag predictions. In addition, the distance between the model centerline and the outer freestream boundary was doubled and no significant difference in base drag was predicted.

Support Interferences

The physics of the support interference need to be recognized whenever wind-tunnel data are used. In general, it has been assumed

and experimentally confirmed that base pressure may be altered by the support for three-dimensional, sting-mounted models.[1,6,11] The rear support usually obstructs the model centerline base flowfield when the nozzles are closely allocated or the plumes are highly underexpanded (although such an arrangement is generally satisfactory for acquiring forebody drag data). The windshield (the end of the constant-diameter portion of the rear sting, also known as chuck or flare) and the sting support may increase the base pressure due to the effects of the compression corner and nose compression, respectively, when the freestream speed is supersonic or transonic. The front support usually decreases the base pressure due to its wake formation. Although magnetic suspension is not an option for a full-vehicle model with engine-on plume effects, the support interference can be minimized with careful general base design and operating condition selection. The cold-flow test data selected in this study fall into such a category. Although a rear sting was used, the base layout, relative exit diameter of the nozzle to the base dimension, and engine and tunnel operating conditions are such that the aspiration base-flow physics prevails and a central reverse jet was not formed. In addition, the compression effects due to the flare and the support are negligible because subsonic freestream flow is considered. Hence, it is determined and later proved that the wind-tunnel data selected were of benchmark quality. The flight-test data are free of any support interference effects.

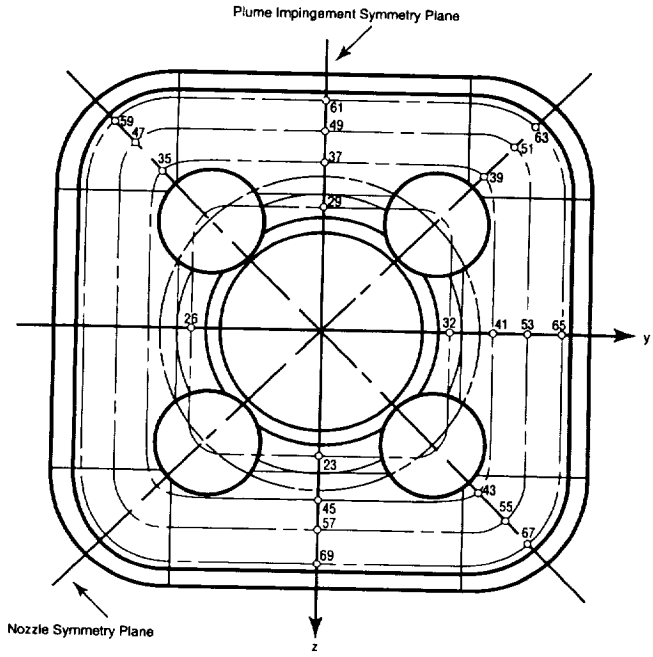

Fig. 4 Pressure transducer locations for subscale cold-flow test.

Results and Discussion

The computations were performed on a NASA MSFC Cray Y-MP. The computational time for a typical cold-flow calculation was estimated as 1.0×10^{-4} CPU s/grid/step. Approximate convergence is reached by tracking not only the flow residuals (when the residual of the vectors was below 1.0×10^{-4} and those of the scalars were under 1.0×10^{-6}), but also the reduced axial force coefficient time history. Figure 4 shows the base pressure transducer locations during the cold-flow testing. For clarity, the base pressures measured on the two symmetry planes were compared. The pressure taps on the forebody and aftbody were spread both axially and azimuthally. The measured pressure does not vary significantly in the azimuthal direction. In the flight tests, only axial drag was estimated from the accelerometer measurement and from the estimations on varying weight and thrust. As such, the reduced data showed scatter with time, in addition to instrumental noise. The average was used, and the uncertainty estimated. Frozen and finite rate chemistry methods were used in the flight-test benchmarks. In finite rate chemistry calculations, the PARASOL method[24] was used to solve the coupled chemistry system. A seven-species, nine-reaction subset[25] was used to depict the finite rate hydrogen-oxygen afterburning kinetics. The computational time for a typical frozen chemistry calculation was estimated as 1.9×10^{-4} CPU s/grid/step. The extra 0.9×10^{-4} CPU s/grid/step came from the overhead for solving the seven-species transport equations. The computational time for a finite rate chemistry calculation is 6.3×10^{-4} s/grid/step. In all of the cases studied, those using the frozen chemistry method underpredicted the base pressure because the afterburning was not modeled.

Cold-Flow Test Cases

During the cold-flow tests, some flow unsteadiness was observed in the base region, as expected for flow over general backward-facing step formations. Observed forebody and aftbody flows were steady. The flow unsteadiness in the base area decreases as the freestream Mach number increases. Figure 5 shows the comparison of base pressure coefficients on two symmetry planes. Case c149b represents cold-flow test number 149 and the last letter, b, indicates grid B

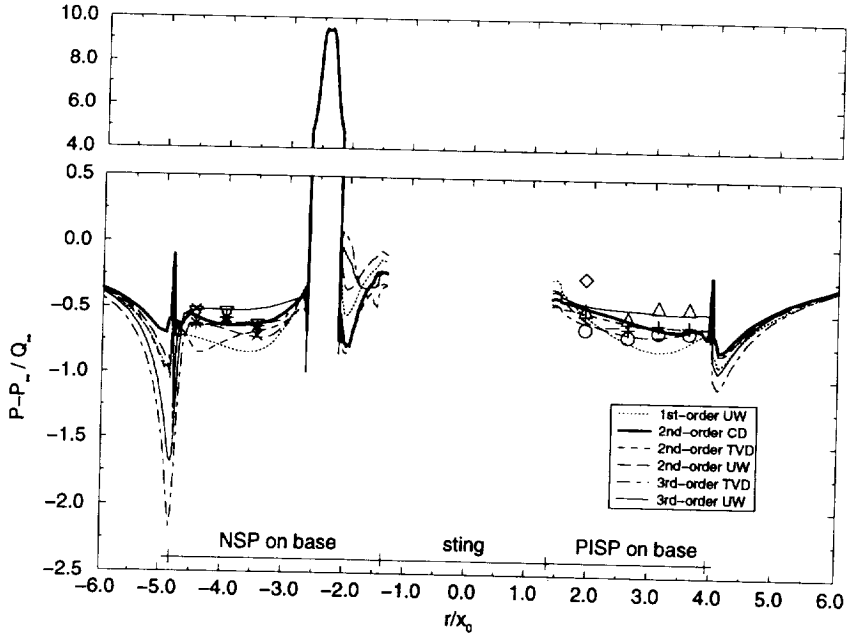

Fig. 5 Comparison of base pressure coefficients on two symmetry planes for c149b: ○, BP29, 37, 49, 61; △, BP32, 41, 53, 65; +, BP23, 45, 57, 69; ◇, BP26; ▽, BP35, 47, 59; ×, BP39, 51, 63; and *, BP43, 55, 67.

was used in the CFD solution, whereas BP29 stands for base pressure tap number 29. The spread of the groups of data taken at 90-deg intervals indicates flow unsteadiness; otherwise the data spread should be minimal. This case was operated at $M_\infty = 0.3$ and $P_e/P_\infty = 30$. There are neither data nor predictions in the central region in which a 3-in.-diam hole was carved to house the sting. The corner expansion can be seen near the outer edge of the base. The predictions also picked up the flow unsteadiness with a maximum amplitude of the base pressure coefficient not exceeding ± 0.015, which is not shown for clarity (the uncertainty band for the data is about ± 0.2). In general, the computed base pressure coefficients for all of the differencing schemes lay within the data band, except for those of the first-order upwind scheme. Note that Q_∞ is a very small number in the low-speed, near atmospheric environment; the discrepancy is, therefore, small in the absolute pressure sense, even for the first-order difference scheme. Among the schemes tested, the second-order CD scheme seems to give the best comparison.

Also shown in the upper graph of Fig. 5, the pressure coefficient profile on the nozzle exit plane is the result of a separate two-dimensional FDNS calculation. The peaks indicate the exiting reflected nozzle shock. The nonuniformity of the nozzle exit pressure profile clearly demonstrates the importance of a separate CFD nozzle calculation over a uniform flow property profile obtained from a one-dimensional calculation.

Figure 6 shows the comparison of forebody and aftbody pressure coefficients. The computed pressure coefficients overlap each other, indicating flow steadiness, for all of the differencing schemes on the two symmetry planes. In general, the computed pressure rises to stagnation pressure at the nose and immediately dips through an expansion, as expected. A second expansion was predicted at the transition from the nose section to the second conic section. On the plume impingement symmetry plane, a third expansion occurs at the transition from the second conic section to the third conic section, followed by a compression near the transition from the conic forebody to the super-circle afterbody. That expansion–compression combination was much less discernible for the nozzle symmetry plane, possibly because the plume impingement symmetry plane intersects the rounded corner of the super-circle, whereas the nozzle symmetry plane passes through the flat side. The pressure then decreases slightly until the end of the aftbody section, where a significant pressure drop develops due to the corner expansion and the base-flow recirculation. Afterward, the pressure recovers to that of ambient. In general, the computed pressure coefficients agreed very well with those of the data, although the third-order schemes predicted a slightly higher ambient pressure coefficient near the computational exit boundary.

Figure 7 shows the comparison of computed axial force coefficient histories against reported test data. The integration area covers all of the aeroshell surface except for the four holes that house the nozzles and one hole that houses the sting. In the wind-tunnel model, the aeroshell was hollow, and the inner pressure force against the inside of aeroshell needs to be subtracted. The aeroshell inside pressure is at the level of base pressure, and an average of three measured pressures located differently was used to reduce the axial drag. Because the total drag is the sum of the forebody, aftbody, and base drags, any base flow unsteadiness would show up in the axial drag. The single measurement ($C_{au} = 0.5134$) appears to be nonoscillatory because it was not taken against time. Typical computed C_{au} history shows steady, short wave oscillations as it approaches a quasisteady state. The first-order UW scheme is most diffusive as evidenced by the overprediction of the final C_{au} and the smallest amplitude in oscillations; whereas less diffusive, second-order UW and TVD schemes both overpredicted the C_{au} slightly. The third-order UW scheme underpredicted the test data. The second-order CD scheme required only 300 iterations to converge around the right value and appears to be the best among the six schemes tested. Third-order TVD predicted the correct level of C_{au} but required more iterations to reach its quasisteady state.

The freestream flow reattached the sting at about a quarter-body length after the base. Because of low P_e/P_∞, aspiration physics dominate in the base region. In fact, even with the existence of the sting, the plume-to-sting impingement did not cause a reversal of the plume boundary flow. The flow reversal behind the base was caused entirely by the interaction between the external flow and the base, although the base environment is influenced by the presence of the plumes.

The computed axial drags were averaged for the last 500 iterations and compared against data in Table 1. It can be seen that the percentage error for the CD scheme for c149b is less than 0.1%.

Table 1 Comparison of C_{au} for the cold-flow tests

Case	M_∞	Scheme	Test	FDNS	|err%|
c141b	0.1	First UW	1.1170	1.2520	12.1
		Second CD		1.1667	4.4
		Second TVD		1.0649	4.6
c149b	0.3	First UW	0.5134	0.6258	21.9
		Second UW		0.5391	5.0
		Second CD		0.5140	0.1
		Second TVD		0.5448	6.1
		Third UW		0.4647	9.5
		Third TVD		0.5168	0.7

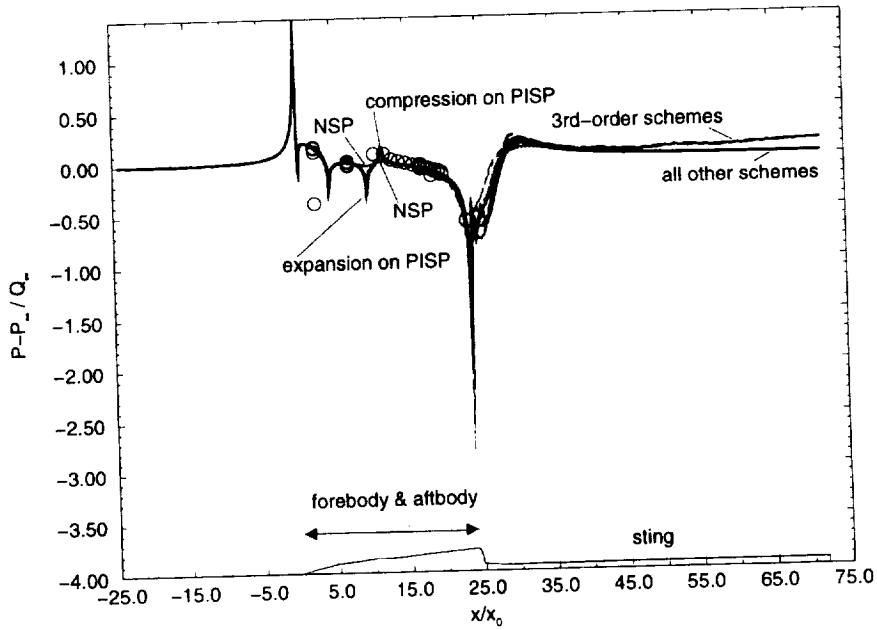

Fig. 6 Comparison of forebody and aftbody pressure coefficients for c149b: O, data.

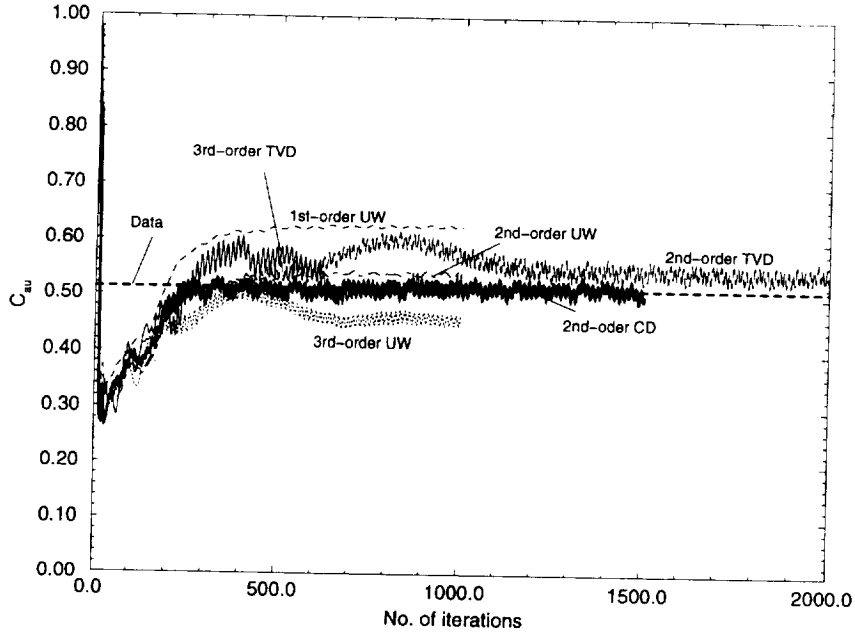

Fig. 7 Comparison of computed C_{au} histories against data for cold-flow test c149b.

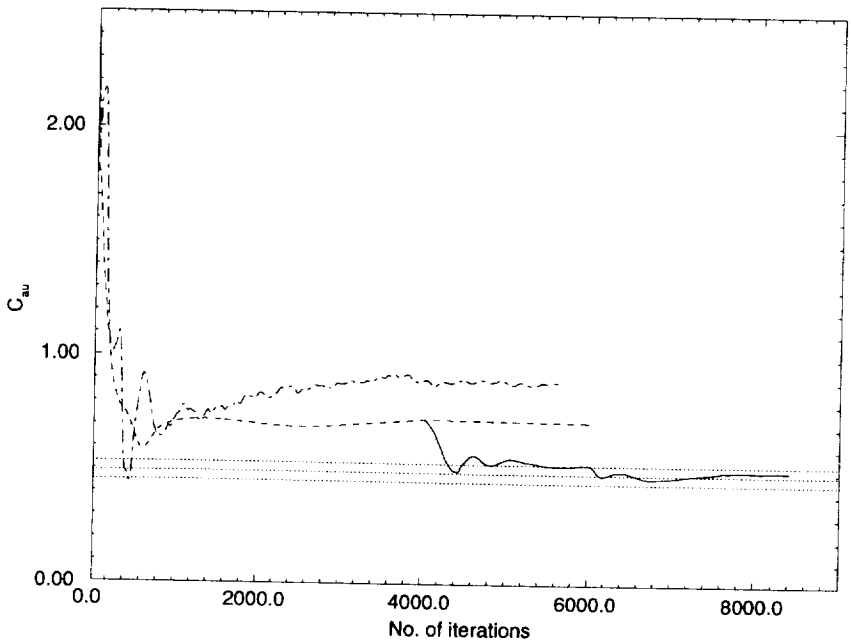

Fig. 8 Comparison of C_{au} histories for flight test case ft8p2: - - - -, ft8p2 data; – – –, grid F, CD, reaction; – – –, grid G, first-order UW, frozen; and ———, grid H, CD, reaction.

In case c141b, the percentage error for the CD scheme is 4.4%, possibly due to higher flow unsteadiness at lower freestream Mach number, and, hence, larger error band for the data. The parametric study also showed that overprediction of axial drag correlates closely with underprediction of base pressures, and vice versa. In summary, the CD scheme seems to yield the best comparison and is chosen for the subsequent flight-test benchmarks. Several cold-flow test benchmarks at high subsonic and transonic freestream flow speeds were performed but not reported because of concern over the sting interference effects. Although in one engine-off ($M_\infty = 0.8$) case the error percentage of the computed C_{au} was less than 4.0%, there was still evidence that compression from the sting chuck had influenced the measured base pressures.

Flight-Test Cases

Three flight-test data points, ft6p1, ft6p2, and ft8p2, were computed. In general, when other parameters were equal, results using frozen chemistry always overpredicted the axial drag, whereas those using finite rate chemistry always had better comparisons, revealing the finite rate characteristic of afterburning. Nevertheless, a frozen chemistry solution can be used to establish an upper bound for the axial force and can also be used as an initial solution for the subsequent finite rate chemistry calculations for its faster convergence. Again, the underprediction of base pressure is associated with overprediction of axial drag. Figure 8 shows the comparison of computed axial force coefficients with that of flight test number 8 data point number 2 (ft8p2) operated at $M_\infty = 0.23$. The drag was overpredicted with grid F (320,787 points), even with a CD scheme and finite rate chemical reactions. The drag prediction was improved with grid G (408,288 points) in which 21 more points were added in the axial direction of the plume afterburning region, even with a first-order UW scheme and with frozen chemistry, both of which tend to increase the predicted C_{au} value. While examining the plume shape through the species concentration and temperature contours plots, it is determined that the grid domain after the base can be shortened at least 30% (to 1.4 body lengths) without increasing the total grid number. Grid H (408,288 points) was thus constructed, essentially adding grid density to the afterburning mixing layers.

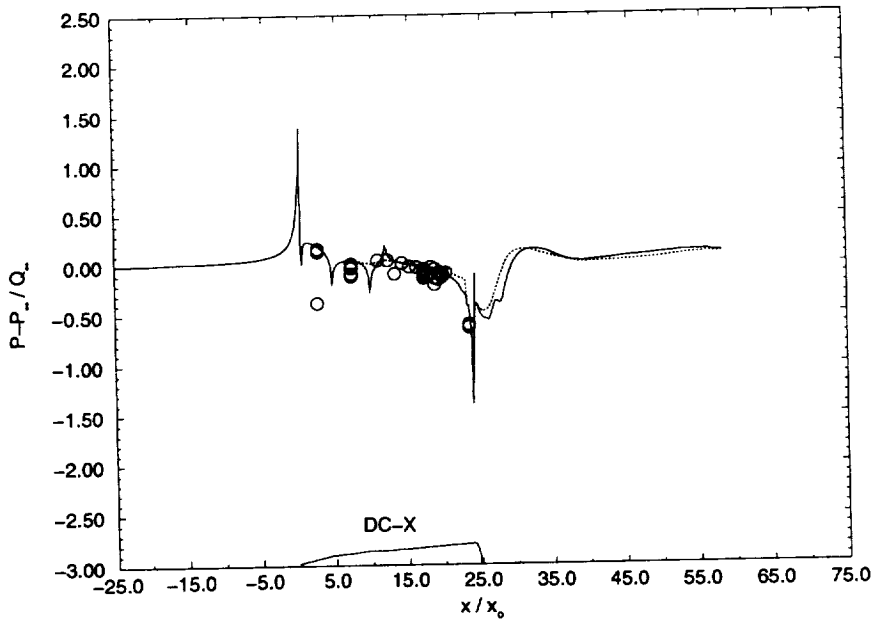

Fig. 9 Comparison of forebody and aftbody pressure coefficients for ft8p2: O, c144 data; ———, grid H, CD, reaction, PISP; and - - - -, NSP.

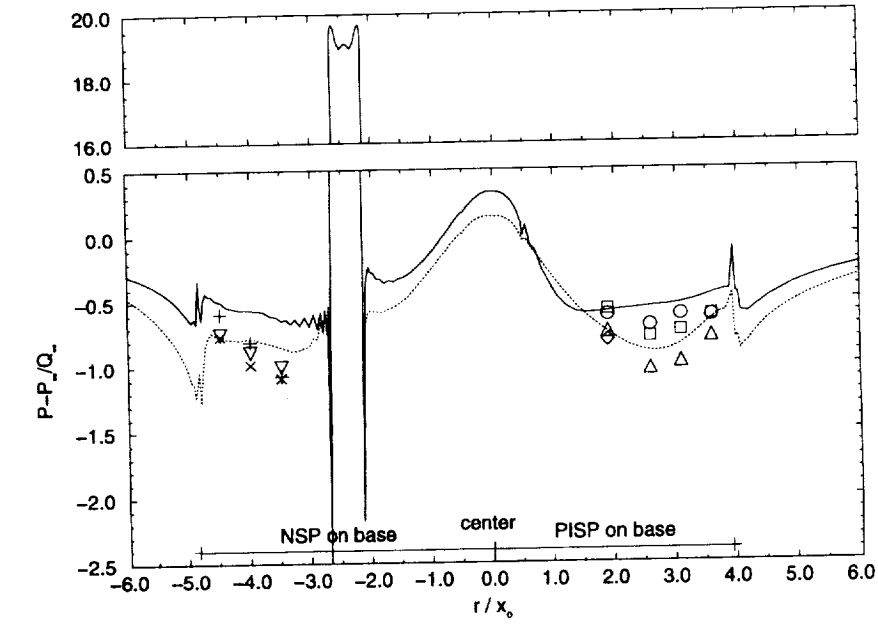

Fig. 10 Comparison of base pressure coefficients on two symmetry planes for ft8p2: symbols identical to those in Fig. 5, c144 data; ———, grid H, CD, reaction; and - - - -, grid G, first-order UW, frozen.

Starting with grid G solution at 4000 iterations, the grid H solution quickly dropped to the upper band of the test data and eventually settled within the uncertainty band of the measurement. Two points may be made here. 1) Grid density that was suitable for cold-flow simulations is not enough for flight-test validations, due to the combustion effect. 2) Adequate grid density in the afterburning region is important in obtaining reasonable base-flow predictions. Compared to cold-flow case c149b, the predicted C_{au} history of the flight-test case does not show much unsteadiness, although both were operated in the subsonic freestream flow region. It is speculated that the bigger, hotter (1940 K) and faster (3230 m/s) plumes in the flight test entrains more air than the thinner, colder (133 K) and slower (1110 m/s) plumes in the cold-flow test; hence, base recirculation is much stabilized in the flight test, even though the nozzle exit Mach numbers (2.6 and 2.5, respectively) were very close.

During flight tests, much less instrumentation is used relative to that of wind-tunnel tests. Figure 9 shows the computed forebody and aftbody pressure coefficients for ft8p2 vs those of a cold-flow test c144, but operated at a similar freestream Mach number and the same chamber-to-ambient pressure ratio. It is interesting to see that they compared very well, indicating the forebody and aftbody flows were not affected by the combusting plumes in this instance, thus implying the forebody drag of a flight vehicle can probably be scaled with that measured from a cold-flow test, if basic scaling criteria are met. The same cannot be said for aftbody drag because most likely it would be affected by the hot-base flows, for example, at higher altitudes. On the other hand, Fig. 10 shows a better comparison of the base pressures between the cold-flow test data and those of flight-test prediction using grid G, first-order UW scheme and frozen chemistry, whereas the flight-test prediction using grid H, reacting flow, and the CD scheme overpredicted the cold-flow test data. However, the grid H solution should match the base pressure better because it matched the axial drag best, indicating the actual base pressures in the flight-test case should have been higher, if measured. The implication is that the base drag of the flight vehicle is probably not scalable with that of the cold-flow test without incurring a certain amount of error. This observation is in agreement with notions that the reacting flow physics is not scalable with the

Table 2 Comparison of C_{au} for the flight tests

Case	M_∞	Scheme	Test	FDNS	|err%|
ft6p1f	0.10	Second CD	1.035	1.0361	0.1
ft6p2g	0.13	Second CD	0.930	0.9125	1.8
ft8p2h	0.23	Second CD	0.490	0.5094	3.9

cold-flow test[5] and afterburning tends to increase base pressures.[11] In addition, the characteristics of the nozzle exit pressure profile, shown in the upper portion of Fig. 10, are completely different from those of cold-flow tests (Fig. 5). For instance, the location of the exiting nozzle shock of the flight-test case is almost at the wall whereas that of the cold-flow test is near the centerline, highlighting the hot-flow effect and the importance of preparing a nonuniform nozzle exit flow profile for accurate prediction of the base-flow physics. Figure 10 also shows the highest base pressures occur at the center $(r/x_0 = 0)$, which is characteristically correct.

Table 2 shows the comparison of predicted axial drags with those of the flight tests. The corresponding altitudes for ft6p1, ft6p2, and ft8p2 are 1400, 1800, and 2800 m, respectively. The grid density requirement increases as altitude increases, as expected due to increased plume expansion. It can be seen that solution-adapted gridding[9] may be required for efficient aerodynamic performance predictions in high-speed, high-altitude regimes. Nevertheless, in the low-speed regime, the comparison between the prediction and test was excellent with the maximum error not exceeding 4%. In summary, with adequate grid density distribution, second-order CD and finite rate afterburning chemistry, FDNS can be used to confidently predict low-speed aerodynamic performance for flight vehicle operations.

Conclusion

A three-dimensional, viscous flow, pressure-based CFD formulation has been validated to characterize the aerodynamic performance of a multiple-engine launch vehicle at subsonic speeds for both the wind-tunnel and flight tests. The CD scheme is found to be most suitable for CFD design calculations in the subsonic flow regime. The computed vehicle total drag, forebody and aftbody, and base surface pressure coefficients compared favorably with those of the available data, indicating current CFD methodology can be used to predict the low-speed aerodynamic performance of a reusable rocket. The scaling practice using cold-flow data inferring flight conditions may not be applicable to the base region whenever the finite rate chemistry effect is significant.

Acknowledgment

This work was performed under the Cooperative Agreement between McDonnell Douglas/Boeing and Marshall Space Flight Center for the Phase I Reusable Launch Vehicle/X-33 Technology Development Program. The authors wish to thank Scott Ward of McDonnell Douglas Aerospace for technical assistance and providing test data for use in this study. The team also wishes to thank Chief Aerodynamicist Werner Dahm for discussions on wind-tunnel physics.

References

[1]Lamb, J. P., and Oberkampf, W. L., "Review and Development of Base Pressure and Base Heating Correlations in Supersonic Flows," *Journal of Spacecraft and Rockets*, Vol. 32, No. 1, 1995, pp. 8–23.

[2]Roberts, B. B., Wallace, R. O., and Sims, J. L., "Plume Base Flow Simulation Technology," *Shuttle Performance: Lessons Learned*, NASA CP-2283, Part 1, March 1983.

[3]Dahm, W. K., "Introduction to the Problem of Rocket Base Heating, and to the Behavior of Liquid Rocket Jet Plumes," *Molecular Radiation and Its Application to Diagnostic Techniques*, NASA TM X-53711, Oct. 1967, pp. 4–16.

[4]Bender, R. L., "Base Flow," *Rocket Exhaust Plume Technology*, edited by T. M. Gililand, Publication 263, Chemical Propulsion Information Agency, 1981, pp. 5.1.1–5.9.101.

[5]Dahm, W. K., "Relevance of Laboratory Experiments to Actual Radiating Flows," *Molecular Radiation and Its Application to Diagnostic Techniques*, NASA TM X-53711, Oct. 1967, pp. 459–473.

[6]Whitfield, J. D., "Support Interference at Supersonic Speeds," AGARD Rept. 300, March 1959.

[7]Gielda, T. P., Walter, T. M., and Agarwal, R. K., "Single Stage Rocket Performance: Prediction and Test," AIAA Paper 92-1386, March 1992.

[8]Wang, T.-S., "Numerical Analysis of Base Flowfield for a Four-Engine Clustered Nozzle Configuration," *Journal of Propulsion and Power*, Vol. 11, No. 5, 1995, pp. 1076–1078.

[9]Wang, T.-S., "Base Flowfield Grid-Resolved Analysis for a Four-Engine Clustered Nozzle Configuration," *Journal of Spacecraft and Rockets*, Vol. 33, No. 1, 1996, pp. 22–29.

[10]Brewer, E. B., and Craven, C. E., "Experimental Investigation of Base Flow Field at High Altitude for a Four-Engine Clustered Nozzle Configuration," NASA TND-5164, Feb. 1969.

[11]Murthy, S. N. B., and Osborn, J. R., "Base Flow Phenomena with and Without Injection: Experimental Results, Theories, and Bibliography," *Aerodynamics of Base Combustion*, edited by S. N. B. Murthy, Vol. 40, Progress in Astronautics and Aeronautics, MIT Press, Cambridge, MA, 1976, pp. 7–210.

[12]Abdol-Hamid, K. S., and Wilmoth, R. G., "Multiscale Turbulence Effects in Underexpanded Supersonic Jets," *AIAA Journal*, Vol. 27, No. 3, 1989, pp. 315–322.

[13]Dash, S. M., and Wolf, D. E., "Interactive Phenomena in Supersonic Jet Mixing Problems, Part I: Phenomenology and Numerical Modeling Techniques," *AIAA Journal*, Vol. 22, No. 7, 1984, pp. 905–913.

[14]Soni, B. K., Thompson, J. F., Stokes, M. L., and Shih, M.-H., "GENIE++, EAGLEView and Tiger: General and Special Purpose Interactive Grid Systems," AIAA Paper 92-0071, Jan. 1992.

[15]Steinbrenner, J. P., and Chawner, J. R., "The GRIDGEN Version 8 Multiple Block Grid Generation Software," MDA Engineering, Rept. 92-01, Arlington, TX, Dec. 1992.

[16]Ames Research Staff, "Equations, Tables, and Charts for Compressible Flow," NACA Rept. 1135, 1953.

[17]Chen, Y.-S., "FDNS—A General Purpose CFD Code," Engineering Sciences, Inc., Rept. ESI-TR-91-01, Huntsville, AL, May 1993.

[18]Wang, T.-S., and Chen, Y.-S., "Unified Navier–Stokes Flowfield and Performance Analysis of Liquid Rocket Engines," *Journal of Propulsion and Power*, Vol. 9, No. 5, 1993, pp. 678–685.

[19]Chen, Y.-S., Liaw, P., Shang, H.-M., and Chen, C.-P., "Numerical Analysis of Complex Internal and External Viscous Flows with a Second-Order Pressure-Based Method," AIAA Paper 93-2966, July 1993.

[20]Chen, Y.-S., and Kim, S. W., "Computation of Turbulent Flows Using an Extended k-ε Turbulence Closure Model," NASA CR-179204, Oct. 1987.

[21]Chen, Y.-S., Cheng, G. C., and Farmer, R. C., "Reacting and Non-Reacting Flow Simulation for Film Cooling in 2-D Supersonic Flows," AIAA Paper 92-3602, July 1992.

[22]Liakopouls, A., "Explicit Representations of the Complete Velocity Profile in a Turbulent Boundary Layer," *AIAA Journal*, Vol. 22, No. 6, 1984, pp. 844–846.

[23]Svehla, R. A., and McBride, B. J., "FORTRAN IV Computer Program for Calculation of Thermodynamic and Transport Properties of Complex Chemical Systems," NASA TN D-7056, Jan. 1973.

[24]Wang, T.-S., Chen, Y.-S., and Farmer, R. C., "Numerical Study of Reactive Ramjet Dump Combustor Flowfields with a Pressure Base CFD Method," AIAA Paper 89-2798, July 1989.

[25]Wang, T.-S., McConnaughey, P., Chen, Y.-S., and Warsi, S., "Computational Pollutant Environment Assessment from Propulsion-System Testing," *Journal of Spacecraft and Rockets*, Vol. 33, No. 3, 1996, pp. 386–392.

B. A. Bhutta
Associate Editor